PHYSICAL REVIEW C VOLUME 44, NUMBER 5 NOVEMBER 1991

Measurement of $A_y(\theta)$ for $n+^{208}$Pb from 6 to 10 MeV and the neutron-nucleus interaction over the energy range from bound states at -17 MeV up to scattering at 40 MeV

M. L. Roberts,* P. D. Felsher, G. J. Weisel, Zemin Chen,† C. R. Howell, W. Tornow, and R. L. Walter
Department of Physics and Triangle Universities Nuclear Laboratory, Duke University, Durham, North Carolina 27706

D. J. Horen
Oak Ridge National Laboratory, Oak Ridge, Tennessee 37831
(Received 6 March 1991)

High-accuracy measurements of $A_y(\theta)$ data for elastic scattering and inelastic scattering to the first excited state for $n+^{208}$Pb have been performed at 6, 7, 8, 9, and 10 MeV. In addition, $\sigma(\theta)$ was measured at 8 MeV. These data provide an important subset for the growing database for the $n+^{208}$Pb system from bound-state energies to energies above 40 MeV, the limit of the range of interest here. This database has been interpreted via several approaches. First, a conventional Woods-Saxon spherical optical was used to obtain three potential representations for the energy range from 4 to 40 MeV: "best fits" at each energy, constant-geometry global fit with linear energy dependences for the potential strengths for the range 4.0–40 MeV, and an extension of the latter model to allow a linear energy dependence on the radii and diffuseness. A preference for a complex spin-orbit interaction was observed in all cases. Second, the dispersion relation was introduced into the spherical optical model to obtain a more "realistic" representation. In our approach, the strength and shape of the real potential was modified by calculating the dispersion-relation contributions that originate from the presence of the surface and volume imaginary terms. Two potentials were developed, one based only on the scattering data (from 4.0 to 40 MeV) and another based additionally on single-particle and single-hole information down to a binding energy of 17 MeV. In addition, the $\sigma(\theta)$ and $A_y(\theta)$ measurements were compared to earlier conventional and dispersion-relation models. One of the latter of these included an l dependence in the absorptive surface term, and we applied this model in the 6- to 10-MeV region to describe all the $\sigma(\theta)$ and the new $A_y(\theta)$. A reasonably good overall description was obtained by all the models; however, only the l-dependent model came close to giving a detailed agreement to the data around 7 MeV, a region where some abnormal angular dependences occur in the data.

I. INTRODUCTION

Since the publication of Mahaux and Ngô [1] in 1982, one of the most intriguing developments in nucleon-nucleus scattering is the gradual recognition of the impact of the dispersion relation which connects the imaginary (absorptive) central potential to the real central potential. The existence of the relation, which occurs because of causality requirements, was pointed out for nuclear systems by Feshbach [2] in 1958, but its importance was ignored in most optical-model analyses. Mahaux and Ngô showed that the dispersion relation (DR) provided a convenient method for interconnecting the shell-model potential for bound states to the nucleon-nucleus potential for scattering in the continuum. They were also able to obtain the Hartree-Fock potential (the mean field) for finite nuclear systems. Their specific examples were neutron scattering from the closed-shell nuclei ^{208}Pb and ^{40}Ca. In the last few years many DR analyses have been published because of the successes illustrated in their paper.

The system ^{208}Pb(n,n) has been central to much of the development of optical-model potentials and, in particular, the inclusion of the dispersion relation. There are numerous reasons for this. First, there exists a wealth of high-accuracy differential cross-section $\sigma(\theta)$ and total cross-section σ_T data over a wide energy range. Second, there also exists a large amount of complementary information about bound states, both particle and hole states, for the $n+^{208}$Pb system. In addition, many phenomenological models have been developed which have shown that ^{208}Pb(n,n) is a good candidate for a spherical-optical-mode (SOM) representation. Last, there is a large amount of complementary ^{208}Pb(p,p) data; this feature permits detailed comparison between models for the two scattering systems and allows investigation of isospin and Coulomb effects.

Detailed information about ^{208}Pb(n,n) elastic-scattering differential cross sections $\sigma(\theta)$ have been obtained in a set of careful measurements performed at Ohio University [3–5]. From a comprehensive analysis of this work in 1985, Annand, Finlay, and Dietrich [5] found that the data set could not be fit at all energies using Woods-Saxon (WS) form factors with constant geometry. The fits to the differential scattering data below $E \approx 20$ MeV required variations in the geometries of the real volume and imaginary surface potentials. In particular, they observed that the real radius increased and the depth of the

real volume potential flattened as the neutron energy decreased from 20 to 5 MeV. This resulted in a volume integral for the real potential that showed an anomaly below 20 MeV similar to what had been predicted by Mahaux and Ngô [1]. In a subsequent paper, Johnson, Horen, and Mahaux (JHM) [6] invoked a DR constrained optical model with fixed geometry to analyze both the scattering and bound-state data and deduced a unified description of the mean field. This work clearly exhibited the changes in the depth and radius of the "effective" real volume potential brought about by the DR. Following this publication, Jeukenne, Johnson, and Mahaux (JJM) [7] expanded this analysis. Although the DR models do a remarkable job of describing most of the data, they do not give precise reproductions of the scattering data, especially in the backward-angle region below 10 MeV.

While the optical models were being developed in the work to be reported in the present paper, Finlay *et al.* [8] presented optical-model analyses of $\sigma(\theta)$ and $A_y(\theta)$ data for ^{208}Pb(p,p) for $9 \leq E \leq 61$ MeV and of $\sigma(\theta)$ for ^{208}Pb(n,n) for $4 \leq E \leq 40$ MeV. In addition to conventional SOM analyses, they performed analyses first involving the dispersion relation (but without considering the bound-state information in the region $E<0$) and then involving non-Woods-Saxon shape potentials via a Fourier-Bessel description. They confirmed the anomalous energy-dependent behaviors of the root-mean-squared radius and the volume integral for the real potential for ^{208}Pb(n,n) for $E<8$ MeV.

At the Triangle Universities Nuclear Laboratory (TUNL), we have developed a time-of-flight system to measure the analyzing power function $A_y(\theta)$ for neutron scattering in the 6–19-MeV energy range. One of our earliest measurements was a determination of $A_y(\theta)$ at 10 and 14 MeV for ^{208}Pb(n,n) by Floyd [9]. Since that time, we have improved our facility for conducting such experiments more efficiently, and this has allowed us the unique capability to obtain detailed shape information of $A_y(\theta)$ with high statistical accuracy. As these techniques were developing, calculations by one of the present authors (D.H.) suggested that the ^{208}Pb(n,n) system would be a good testing ground for parity-dependent potentials, as well as l-dependent potentials, if one had high-accuracy $A_y(\theta)$ data in the 6–10-MeV range. Since this energy region was also the region where Annand, Finley, and Dietrich [3] found interesting energy dependences in their SOM analyses and where the DR was shown to play a particularly sensitive role, we undertook such measurements. In addition, in order to complete the $\sigma(\theta)$ database in the 4.5–10-MeV range, we measured $\sigma(\theta)$ at 8 MeV for ^{108}Pb(n,n). In the process of these measurements, data for $A_y(\theta)$ and $\sigma(\theta)$ for inelastic scattering to the first excited state (3^-) were also obtained.

We note that analyzing power data for neutron scattering in the 6–10-MeV range play an important role in testing nucleon-nucleus scattering models for heavy nuclei. The reason for this is that the complementary piece of information that is indeed useful at higher energies, i.e., scattering observables for ^{208}Pb(p,p) are almost completely described by the Coulomb scattering process. For instance, all the detailed information about the nucleon-nucleus spin-orbit interaction is completely masked for ^{208}Pb(p,p) below 10 MeV.

The presentation here is organized in the following way. Details of the experimental techniques and procedures for data analyses and uncertainties are described in Secs. II and III, respectively. Conventional spherical-optical-model analyses for ^{208}Pb(n,n) over the energy range from 4.0 to 40 MeV are detailed in Sec. IV. The SOM analyses are extended to include the dispersion relation in Sec. V, where eventually the single-particle information is fit along with the data set for (n,n) scattering. A brief summary is given in Sec. VI. In this section we also compare the data with calculations using the DR models of JHM and JJM. (By the time the paper of Finlay *et al.* [8] appeared, all the conventional SOM and some of the DR calculations reported in the present paper had been completed [10]. The database in the present paper is larger than in Ref. [8], and differences in the derived parameters are attributed in part to the improved database and in part to the relative weights given to different data sets in the fitting procedure.)

II. EXPERIMENTAL TECHNIQUES

A. Introduction

Differential cross sections $\sigma(\theta)$ and analyzing powers $A_y(\theta)$ were measured using the neutron time-of-flight facilities at TUNL. With the exception of the ion source used, both types of measurements utilized similar or identical equipment and followed somewhat similar procedures. Since much of the time-of-flight equipment and procedures have been documented elsewhere [11,12], this paper will only give detailed descriptions for the techniques that are new or particularly important in relation to the high accuracy of the data.

B. Cross-section measurement

For the $\sigma(\theta)$ measurement at 8 MeV, a direct-extraction negative-ion source was used to produce a 50-keV dc deuteron beam. The deuteron beam was accelerated by a model FN tandem Van de Graaff accelerator. The ^{2}H$(d,n)^3$He reaction at 0° was used as the source of neutrons. Prior to acceleration, the deuteron beam was chopped and bunched to obtain 1.5-ns pulses at the deuterium-gas target. The beam of pulsed deuterons ($E_d=4.7$ MeV) had a time-averaged intensity of 2 μA at the pulse repetition rate of 2 MHz. The neutron energy spread due to the energy loss of the deuterons in the 6 atm cm of deuterium gas was 180 keV. Three cylindrical scattering samples were used: ^{208}Pb, a standard carbon, and a standard polyethylene. The samples were suspended by a thin steel wire with their axes of symmetry perpendicular to the horizontal scattering plane. The distance from the center of the gas cell to the center of a sample was 12.4 cm. The ^{208}Pb sample contained 116 g and was 3.25 cm high by 2.0 cm in diameter. It had an enrichment of 99.7%.

For $\sigma(\theta)$ measurements the time-of-flight spectrometer facility consisted of four neutron detectors: two main

detectors a neutron-flux monitor, and a pulse-timing monitor. The arrangement of the two main detectors relative to the scattering sample is shown in El-Kadi [11] and is similar to that shown below in Sec. II C. The detectors were cylindrical liquid organic scintillators that allowed good pulse-shape discrimination between events induced by neutrons and γ rays.

The main right and left detectors were heavily shielded, and tungsten shadow bars (at least 50 cm long) were positioned so that the detector, the front edge of the detector collimator, and much of the detector casing were shielded from the direct flux of source reaction neutrons. Flight paths of 2.9 and 3.9 m were used for the right and left detectors, respectively. (Use of the designation *right* corresponds to the case of the incident particles scattering to the right side in a horizontal scattering plane, viewed from above.) The neutron-flux monitor was suspended from the ceiling of the target room and was used to monitor the flux from the source reaction. The pulse-timing monitor was located near 0° reaction angle.

Standard time-of-flight and pulse-shape-discrimination electronics were employed. An energy bias of about 2 MeV was used on the main detectors. Data acquisition and storage was controlled using a Digital Equipment Corporation VAX-11/780 computer.

The $\sigma(\theta)$ measurements were made from 16° to 40° in 4° increments and from 45° to 160° in 5° increments. Data taken with the ^{208}Pb sample in place were referred to as "sample-in" data, while data accumulated with an empty wire hanger in place were referred to as "sample-out" data. From 16° to 40° both detectors were used to obtain measurements at the same scattering angle simultaneously, with one detector on each side of the beam axis. Such measurements were useful in checking for normalization differences between the two detectors and for recognizing and canceling out scattering-angle shifts. Such angle shifts can be caused by beam-steering effects or a misaligned scattering sample. [In the forward-angle region, a slight scattering-angle shift can give noticeably different measured cross sections. For example, near 16°, a change of 0.5° at 8.0 MeV produces a 4.6% change in $\sigma(\theta)$.]

At the beginning, middle, and end of the angular distribution measurement, the yield for neutron scattering from hydrogen was measured for normalization purposes and as a check of systematic drifts in the system. These normalization measurements were made by successively scattering from a polyethylene sample and a carbon sample. The measurements were made at an angle ($\theta_{\rm lab} \approx 30°$) chosen to maximize the separation of the hydrogen-scattering peak from the elastic- and inelastic-scattering peaks of carbon. Incidental to the elastic-scattering data, which is the focus of the present study, data were extracted for inelastic scattering to the first excited state ($J^\pi = 3^-$, $Q = 2.614$ MeV).

C. Analyzing power measurements

For the $A_y(\theta)$ measurements the Lamb-shift polarized-ion source produced a polarized beam of deuterons. The beam was ramped within the source, bunched, and chopped to obtain a pulsed deuteron beam. The polarization transfer reaction ^{2}H($\vec{d},\vec{n}$)^{3}He at 0° served as the source of polarized neutrons. The polarization of the deuteron beam was determined by the quench-ratio method, which has been discussed by Ohlsen and Keaton [13]. The polarization of the neutrons was determined from the measured deuteron-beam polarization using the polarization transfer function determined by Lisowski *et al.* [14].

The beam of pulsed polarized deuterons typically had a time-averaged intensity of 150 nA and a vector polarization of about 65%, of which approximately 90% was transferred to the neutron beam. The repetition rate of the beam bursts was 4 MHz, and the pulses had a full width at half maximum (FWHM) of less than 2 ns. The deuterium-gas thickness ranged from 7.5 atm cm for 6-MeV neutron production to 20 atm cm for 10-MeV neutrons. The respective energy spreads were 0.35 and 0.44 MeV. The same ^{208}Pb scattering sample as was employed in the $\sigma(\theta)$ measurements was used here.

For the $A_y(\theta)$ measurements, the time-of-flight spectrometer facility consisted of six heavily shielded detectors. All of the detectors were liquid organic scintillators and provided good pulse-shape discrimination. The detectors, which are shown in Fig. 1, were arranged in three pairs, each pair consisting of a detector placed at an equal angle of the left and right sides of the incident beam axis. Simultaneous measurements with detectors placed at equal angles help to minimize instrumental asymmetries.

The detector pair 1 and associated shadow bars were also used for the $\sigma(\theta)$ measurement. The minimum and maximum angles for simultaneous measurements when both of these detectors were at equal angles were 16° and 159°, respectively. Flight paths of 3.0 and 3.9 m were used for the right and left detectors, respectively.

Detector pairs 2 and 3 employed copper and polyethylene shadow bars. They were used over an angu-

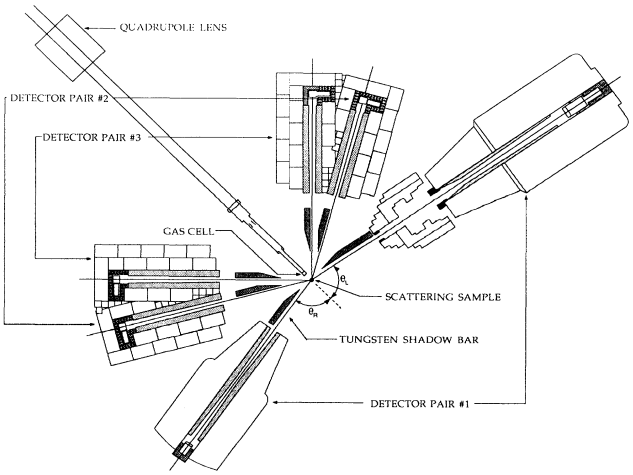

FIG. 1. Arrangement of the six main neutron detectors for the $A_y(\theta)$ measurement.

lar range of 105°–149° and 120°–164°, respectively. All four detectors used in pairs 2 and 3 were rectangular in shape. Pair 2 detectors were 7.6 cm wide, 12.7 cm tall, and 5.1 cm thick and were placed at a flight path of 2.6 m. Pair 3 detectors were 7.6 cm wide, 15.2 cm tall, and 5.1 cm thick and were placed at a flight path of 2.7 m. The overall time resolution, including the effects of the neutron energy spread, was about 3.4 ns at $E=6.0$ MeV and about 2.6 ns at $E=10.0$ MeV.

The $A_y(\theta)$ measurements were made from 16° to 40° in 4° increments and from 45° to 160° in 5° increments. Data were accumulated for four experimental configurations: sample-in spin up, sample-in spin down, sample-out spin up, and sample-out spin down, where "spin up" and "spin down" refer to the polarization direction of the incident neutron beam. The direction of the spin of the incident neutron beam was inverted about every 20 min by changing the direction of the deuteron polarization at the polarization-ion source. The deuteron-beam polarization was measured about every 10 min.

The counting statistics obtained ranged from 0.6% to 3.3% and depended on $\sigma(\theta)$. The measuring times ranged from 1 to 12 h, the latter to obtain a 3.3% statistical uncertainty at 6.0 MeV at $\theta_{lab}=130°$. Since the cross section for inelastic scattering to the first excited state of ^{208}Pb is small compared with the elastic-scattering cross section, analyzing power values for inelastic scattering from the first excited state of ^{208}Pb had much larger statistical uncertainties, ranging from 4.5% to 27%.

III. DATA REDUCTION AND PRESENTATION

A. Cross-section measurements

1. Neutron-yield extraction

To obtain $\sigma(\theta)$ data, neutron yields were extracted from so-called difference spectra (DIFF), which were obtained by subtracting normalized sample-out time-of-flight spectra (OUT) from the corresponding sample-in spectra (IN). Examples of an IN, a normalized OUT, and a DIFF spectrum are shown in Fig. 2. Estimated background levels were drawn in the difference spectra to account for sample-correlated backgrounds that were not measured in the sample-out count. In most cases a linear function adequately described the residual background. Wide windows were chosen about peaks of interest, and a yield per monitor event was calculated. Absolute differential cross sections were determined by comparing the yields for ^{208}Pb to yields for hydrogen scattering and then normalizing to published n-p scattering cross sections [15].

2. Finite-geometry, attenuation, and multiple-scattering corrections

Neutron time-of-flight measurements typically require large samples and detectors, and so the effects of finite geometry, flux attenuation and multiple scattering on the observed yield must be considered. Corrections have been calculated with the TUNL Monte Carlo code EFFIGY15, which simulates the experiment in the laboratory system and calculates corrections to the data using an iterative procedure. In each iteration of the process, the simulation employs a library of total and differential cross sections to generate time-of-flight spectra at each detector angle. When sufficient histories have been obtained, values generated from the current $\sigma(\theta)$ library are used with yields calculated from the simulated time-of-flight spectra to generate correction factors. The correction factors are applied to the experimental data to obtain corrected $\sigma(\theta)$ values. After each iteration calculated yields are compared to experimental yields to check for convergence. Convergence is said to occur when both agree to within a set percentage. If convergence is not achieved, the cross-section library is updated with coefficients from a Legendre polynomial fit to the corrected experimental data of the present iteration, and the iteration process continues. The code EFFIGY15 also calculates the mean energy of the incident neutrons and the mean scattering angles.

The significance of attenuation, finite geometry, and multiple-scattering corrections is seen in Fig. 3. The

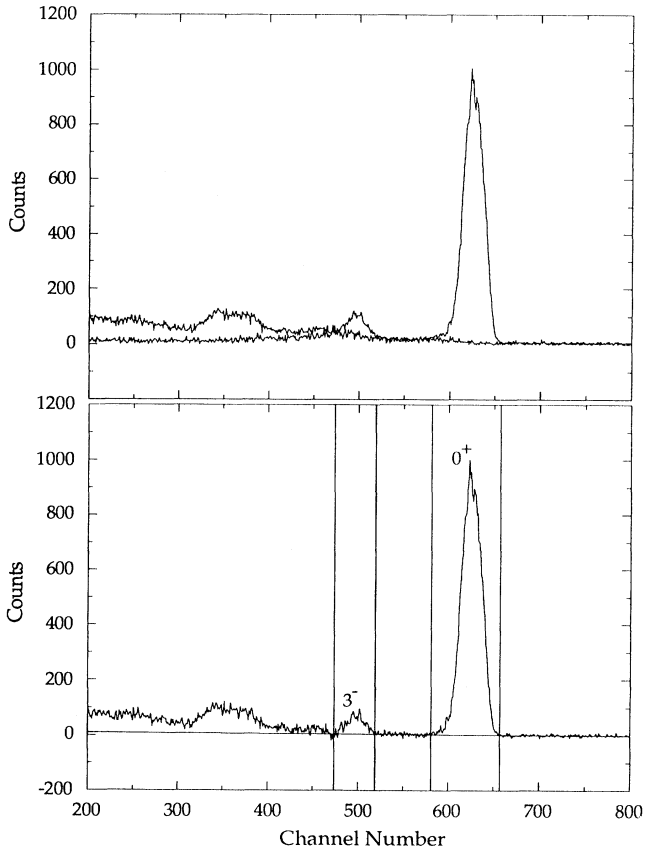

FIG. 2. IN, OUT, and DIFF spectra for the scattering of 8.0-MeV neutrons from ^{208}Pb for $\theta=85°$. Note the offset for zero counts. The peaks for elastic and inelastic scattering are labeled 0^+ and 3^-, respectively. In the difference spectrum, the nearly horizontal solid line is the estimate of the sample-correlated background in the region of the peaks and the vertical lines indicate the two summing windows.

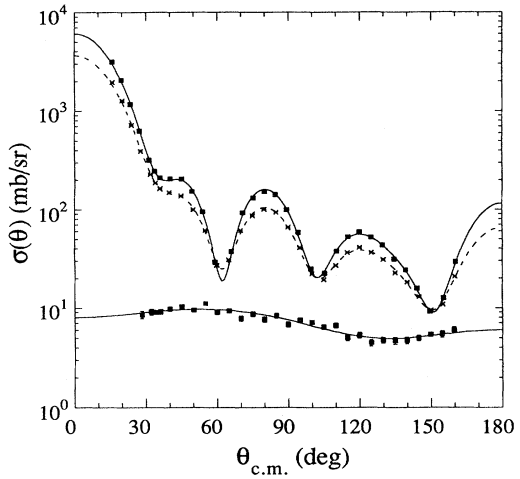

FIG. 3. Top: attenuation, finite-geometry, and multiple-scattering corrections to elastic-scattering data at 8.0 MeV. Normalized yields, uncorrected for attenuation, finite geometry, or multiple scattering, are indicated by ×. The dashed curve is a Legendre polynomial fit. The $\sigma(\theta)$ obtained after EFFIGY corrections are indicated by the squares; the solid curve is a Legendre polynomial fit. Bottom: corrected $\sigma(\theta)$ data for inelastic scattering from the first excited state. The curve is a Legendre polynomial fit.

dominant correction is the flux attenuation of scattered neutrons as they traverse the scattering sample; this causes a lowering of the experimental yields by approximately the same factor across the entire distribution. As expected, corrections for finite geometry and multiple scattering tend to deepen the valleys in the vicinity of $\sigma(\theta)$ minima and sharpen the peaks in the vicinity of $\sigma(\theta)$ maxima.

3. Uncertainties and final data

Two types of errors or uncertainties are associated with the $\sigma(\theta)$ data: relative and normalization. Relative errors represent uncertainties in the shape of the distributions. These errors include the statistical uncertainties from neutron-scattering yields and uncertainties in the relative detector efficiencies and multiple-scattering corrections. Relative errors vary from 3% to 5% for elastic scattering and from 3% to 9% for inelastic scattering. The normalization uncertainty represents a scale uncertainty. It includes uncertainties in yields from n-p scattering used for normalization purposes, analytic corrections applied to n-p scattering yields, n-p cross sections, and the ratio of the number of hydrogen atoms in the polyethylene scatter to the number of ^{208}Pb atoms. The combined error for all these effects is estimated to be 3%.

The quoted uncertainty in $\sigma(\theta)$ data does not include the contribution from the uncertainty in the angular position of the detector relative to the incident-beam axis. We estimate that our angular uncertainty is $\pm 0.1°$. A change of $+0.1°$ typically causes an increase only of about 0.2% in the above relative errors at forward-scattering angles where the slope of $\sigma(\theta)$ is relatively large; this is the worst case. Finally, the mean energy of 7.97 MeV (hereafter called 8.0 MeV) for the neutron beam is believed to be known to within 60 keV.

The corrected $\sigma(\theta)$ data for elastic scattering and inelastic scattering to the first excited state are shown in Fig. 3 compared with expansions in terms of Legendre polynomials. The values shown are for the center-of-mass system. The error bars only represent the relative uncertainties.

B. Analyzing power measurements

1. Calculation of analyzing powers

The difference spectra for the $A_y(\theta)$ measurements were similar to the time-of-flight spectra shown for the $\sigma(\theta)$ measurements, except that the statistical fluctuations were larger. In contrast to the $\sigma(\theta)$ case, where all good neutron events had to be included in the chosen window, narrow windows were set about the peaks of interest in $A_y(\theta)$ spectra in order to optimize the signal-to-noise ratio. Four yields are obtained: left-detector spin up (Y_{LU}), left-detector spin down (Y_{LD}), right-detector spin up (Y_{RU}), and right-detector spin down (Y_{RD}). These yields are combined to obtain the quantity $\alpha(\theta)$ as follows:

$$\alpha(\theta)=\left[\frac{Y_{\mathrm{LU}}(\theta)}{Y_{\mathrm{LD}}(\theta)}\frac{Y_{\mathrm{RD}}(\theta)}{Y_{\mathrm{RU}}(\theta)}\right]^{1/2}. \quad (1)$$

Analyzing power values A_y^{obs} are calculated from $\alpha(\theta)$ using the formula

$$A_y^{\mathrm{obs}}(\theta)=\frac{1}{p_n}\left[\frac{\alpha-1}{\alpha+1}\right], \quad (2)$$

where p_n is the polarization of the neutron beam.

2. Finite-geometry, attenuation, and multiple-scattering corrections

The observed analyzing power $A_y^{\mathrm{obs}}(\theta)$ was corrected for effects due to finite geometry, attenuation, and multiple scattering using a TUNL version of a Monte Carlo code JANE (written by Woye [16]). The code simulates the experiment in the laboratory system and calculates corrections to $A_y^{\mathrm{obs}}(\theta)$ using an iterative procedure. Since JANE must distinguish scattering to the left from scattering to the right and keep track of the neutron polarization after successive scattering processes, the procedure for correcting $A_y(\theta)$ data is more complicated than that for correction $\sigma(\theta)$ data. We will briefly outline our method here. A more detailed description of similar corrections is given in Byrd *et al.* [17].

Because of the combination of the finite sizes of the neutron source, scattering sample, and detector, the observed analyzing power is the analyzing power averaged over a range of angles. The mean width of the distribution of scattering angles is approximately 6°. This large width is mainly due to the scattering angle subtended by the sample as seen by the neutron source. The mean

scattering angle differs from the nominal scattering angle because $\sigma(\theta)$ changes for different regions of the scatterer and because the attenuation shifts the effective center of the scatterer closer to the neutron source.

Thus the results from JANE include both a change in the magnitude of $A_y^{\rm obs}(\theta)$ because of attenuation and multiple scattering and a shift from the nominal scattering angle. The largest correction factors occur where both $\sigma(\theta)$ and $A_y(\theta)$ are changing rapidly with angle. The effect discussed by Tornow *et al.* [18] of an instrumental asymmetry caused by an apparent shift in the center of the scattering sample due to the analyzing power in the ^{2}H$(d,n)^3$He source reaction was not included here, as it is negligible compared to the statistical uncertainties.

The simulation using JANE is as follows. (See also Roberts [10].) Employing a library of analyzing powers, total and differential cross sections, and the physical parameters of the experiment, time-of-flight spectra were generated for each angle. Successive iterations with JANE were performed and the $A_y(\theta)$ library updated after each iteration. Convergence is reached when the corrected $A_y(\theta)$ of the present iteration do not disagree significantly from the corrected $A_y(\theta)$ of the previous iteration. In practice, only three iterations of JANE were usually needed to achieve convergence. The significance of finite-geometry and multiple-scattering corrections applied to $A_y^{\rm obs}(\theta)$ data to obtain $A_y(\theta)$ is shown in Fig. 4 for $E=8.0$ MeV. One notes that the dominant effect of multiple scattering is to decrease the magnitude of the experimentally observed analyzing power. This happens because the contribution from multiply scattered neutrons typically yields a smaller analyzing power.

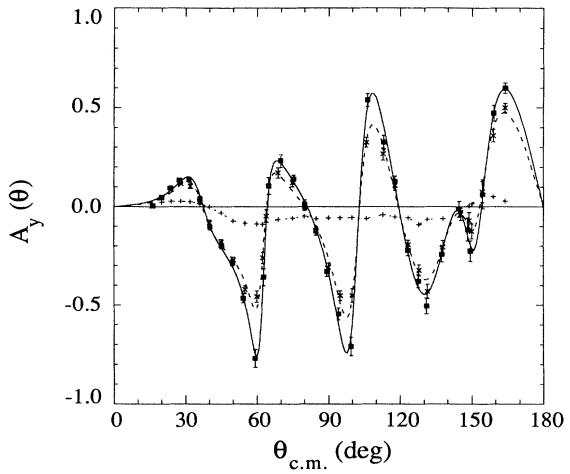

FIG. 4. Attenuation, finite-geometry, and multiple-scattering corrections to $A_y^{\rm obs}(\theta)$ data at 8.0 MeV. Experimentally observed analyzing powers are indicated by $\times$, and the dashed curve is an associated Legendre polynomial fit. Double-scattering analyzing powers, calculated with JANE, are represented by plus signs and are connected by a dotted line. Final single scattering $A_y(\theta)$ are represented by solid squares, and the solid curve is an associated Legendre polynomial fit. Note that the largest corrections occur when both $\sigma(\theta)$ and $A_y(\theta)$ are changing rapidly.

3. *Uncertainties and final data*

The uncertainties for the present $A_y(\theta)$ data also fall into two categories: relative and normalization uncertainties. Relative errors represent uncertainties in the shape of the distributions and vary from about 1% to 9% for elastic scattering and from 6% to 35% for inelastic scattering. These uncertainties include the combined statistical and background uncertainties. The uncertainty in the multiple-scattering corrections was generally computed to a statistical accuracy such that the uncertainty in the corrections themselves had a negligible effect on the quoted final uncertainties. However, when the multiple-scattering corrections were applied to $A_y^{\rm obs}(\theta)$ data, the uncertainties for $A_y(\theta)$ increased accordingly.

Normalization or scale uncertainty includes uncertainties in the deuteron-beam polarization and knowledge of the tensor analyzing powers and vector polarization transfer coefficients for the ^{2}H$(d,n)^3$He reaction at 0°. We estimate that these uncertainties combine to produce an overall uncertainty in the neutron polarization that ranges between ±0.02 and ±0.03.

The mean energy of the incident neutron beam was known to within 0.8%.

After the $A_y^{\rm obs}(\theta)$ were corrected for attenuation, finite geometry, and multiple scattering, the extracted $A_y(\theta)$ were described in the center-of-mass system with functions that were derived from fitting an associated polynomial expansion to the product $A_y(\theta,E)\sigma(\theta E)$ according to

$$A_y(\theta,E)\sigma(\theta,E)=\sum_{l=1}^{n} B_l(E)P_l^1(\cos\theta)\ . \tag{3}$$

This standard procedure is followed in order to locate gross internal inconsistencies in the data. The discrete values for $\sigma(\theta,E)$ used in calculating these fits were determined from Legendre polynomial fits to $\sigma(\theta)$ data, as previously mentioned.

Analyzing powers at 5.97, 6.97, 7.96, 8.96, and 9.95 MeV (hereafter referred to as 6.0, 7.0, 8.0, 9.0, and 10.0 MeV, respectively) for elastic neutron scattering are shown in Fig. 5. Figure 6 shows an expanded comparison of the 10.0-MeV $A_y(\theta)$ data to data previously measured at TUNL by Floyd *et al.* [9]. The $A_y(\theta)$ data for inelastic scattering from the first excited state are shown in Fig. 7. The curves shown in Figs. 5–7 are fits based on Eq. (3). Error bars shown in the figures include only relative uncertainties.

4. *Effect of compound-nucleus contributions on* $A_y(\theta)$

Since the models used later in this work predict only shape-elastic-(SE) scattering observables, compound-nucleus (CN) contributions to $\sigma(\theta)$ and $A_y(\theta)$ must be considered. The effect of the CN contribution is to dilute the structure of the shape-elastic contribution. In the present work, the energy spread was large enough that effects of many CN states were averaged over. Thus we

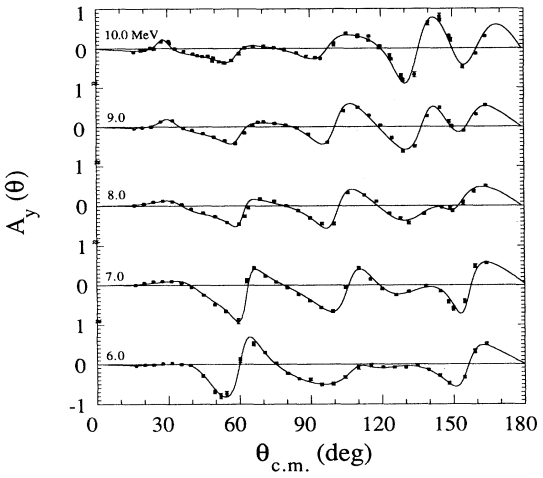

FIG. 5. $A_y(\theta)$ for elastic neutron scattering from ^{208}Pb. The curves are derived from associated Legendre polynomial fits. The data shown at 10.0 MeV include data measured by Floyd *et al.* [9] (see Fig. 6.)

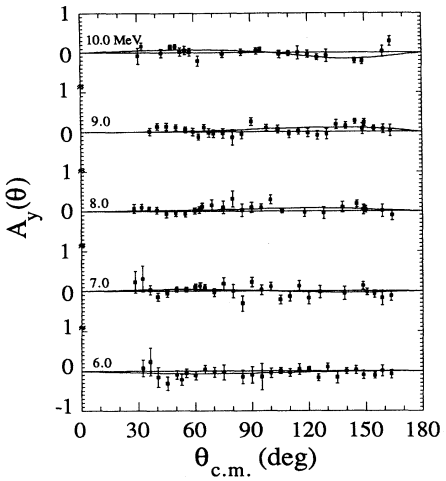

FIG. 7. Analyzing powers for inelastic neutron scattering from the first excited state of ^{208}Pb. The curves are derived from associated Legendre polynomial fits.

corrected for the compound-elastic (CE) contribution according to the simple relation

$$A_y^{\mathrm{SE}}(\theta)=\frac{\sigma(\theta)}{\sigma^{\mathrm{SE}}(\theta)}A_y(\theta)\ , \tag{4}$$

where

$$\sigma(\theta)=\sigma^{\mathrm{SE}}(\theta)+\sigma^{\mathrm{CE}}(\theta)\ . \tag{5}$$

For the elastic-scattering $A_y(\theta)$ data at 8.0, 9.0, and 10.0 MeV, the effects of CE scattering are negligible according to the calculation of Annand, Finlay, and Dietrich [3], and so these data were left unchanged. For the data at 6.0 and 7.0 MeV, corrections were applied using the CE cross sections presented in Annand, Finlay, and Dietrich. Figure 8 shows the CN effects at 6.0 MeV; the CN effects at 7.0 MeV were much smaller.

IV. CONVENTIONAL OPTICAL-MODEL ANALYSIS

A. Form of the optical model

The analysis utilized a spherical optical model (SOM) with potential shapes based on the Woods-Saxon (WS) form

$$f_{\mathrm{WS}}(r,R_i,a_i)=\frac{1}{1+\exp[(r-R_i)/a_i]} \tag{6}$$

and the derivative Woods-Saxon form

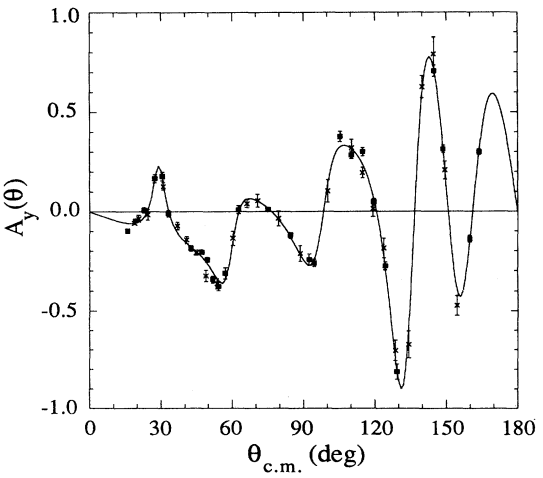

FIG. 6. Expanded view of the present 10.0-MeV data (solid squares) compared to measurements of Floyd *et al.* [9] (represented by ×). The curve is derived from an associated Legendre polynomial fit to the combined sets of data.

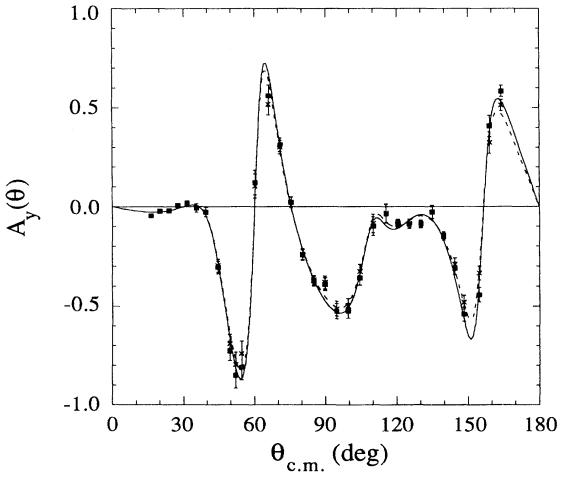

FIG. 8. Effects of CN contributions at 6.0 MeV. Measured $A_y(\theta)$ are indicated by ×, and the dashed curve is derived from an associated Legendre polynomial fit. Shape-elastic $A_y(\theta)$ are indicated by solid squares; the solid curve is derived from an associated Legendre polynomial fit.

$$g_{\rm WS}(r,R_i,a_i)=-4a_i\frac{d}{dr}f_{\rm WS}(r,R_i,a_i)\ . \tag{7}$$

Here the radius parameter is given by $R_i=r_i A^{1/3}$ and diffuseness by a_i. The SOM is then written as

$$\begin{aligned}U(r)=&-V_V(E)f_{\rm WS}(r,R_V,a_V)\\&-i[W_V f_{\rm WS}(r,R_I,a_I)+W_S g_{\rm WS}(r,R_I,a_I)]\\&+2(V_{\rm s.o.}+iW_{\rm s.o.})\left[\frac{1}{r}\frac{d}{dr}f_{\rm WS}(r,R_{\rm s.o.},a_{\rm s.o.})\,\boldsymbol{l}\cdot\boldsymbol{\sigma}\right],\end{aligned} \tag{8}$$

where the successive terms are the real central potential (volume form), imaginary central potential (composed of a volume and a surface peaked form) and spin-orbit potential (composed or real and imaginary parts with identical radii and diffusenesses).

Surface peaking of the imaginary potential is most prominent for low-energy nucleon scattering, while at higher energies the imaginary potential is dominated by volume absorption. The spin-orbit potential is surface peaked and can be complex, but the imaginary part has traditionally been neglected for $E<40$ MeV. One reason for this neglect is that, until recently, $A_y(\theta)$ data for neutron scattering was not sufficiently accurate to explore the strength of $W_{\rm s.o.}$.

B. Summary of database

Differential neutron-scattering data used in the analysis came from three facilities. Differential cross sections were measured at TUNL at 8.0 MeV (present work) and at 10.0, 14.0, and 16.9 MeV by Floyd [9]. In addition, $\sigma(\theta)$ data were obtained at Ohio University at 4.0, 4.5, 5.0, 5.5, 6.0, 6.5, and 7.0 MeV by Annand, Finlay, and Dietrich [3], at 20.0, 22.0, and 24.0 MeV by Finlay *et al.* [4], at 9.0, 11.0, and 25.7 MeV by Rapaport *et al.* [5], and at Michigan State University at 30.3 and 40.0 MeV by De Vito [19]. The 4.0–7.0-MeV ^{208}Pb differential cross sections, as adjusted by Annand, Finlay, and Dietrich for CN contributions, were used for the optical-model fitting.

The analyzing power data, which were all obtained at TUNL, were from the present work at 6–10 MeV and from Floyd [9] at 10.0 and 14.0 MeV.

Average total cross-section values σ_T for $^{\rm nat}$Pb (52% ^{208}Pb) were communicated to us by Larson, Hetrick, and Harvey [20] from 4.0 to 80.0 MeV in steps of 2.0 MeV. The σ_T values at intermediate energies (i.e., 7.0, 9.0, 11.0 MeV, etc.) were obtained through interpolation. An uncertainty of 3.0% was assigned the σ_T values for the fitting process. (Following this stage of the analysis, Schutt *et al.* [21] reported σ_T from 2 to 250 MeV. Their data up to 80 MeV are illustrated in a later section.)

C. Analysis of the scattering data

1. Introduction

For the present calculations, iterations of the SOM parameters were performed using a modified version of the search code GENOA (originally obtained from F. Perey of Oak Ridge National Laboratory). The code was modified at TUNL to include the effects of the Mott-Schwinger electromagnetic interaction [22]. The code calculates cross sections and analyzing powers from a one-body Schrödinger equation using the chosen potential $U(r)$; relativistic corrections are not included. At each stage of the iteration process, for each energy where $\sigma(\theta)$, $A_y(\theta)$, and σ_T data exist, GENOA calculates chi square (χ^2) defined through the relation

$$\begin{aligned}\frac{\chi^2}{N}=&\frac{1}{N_\sigma}\sum_{i=1}^{N_\sigma}\left[\frac{\sigma^{\rm expt}(\theta_i)-\sigma^{\rm calc}(\theta_i)}{\Delta\sigma^{\rm expt}(\theta_i)}\right]^2\\&+\frac{1}{N_A}\sum_{i=1}^{N_A}\left[\frac{A_y^{\rm expt}(\theta_i)-A_y^{\rm calc}(\theta_i)}{\Delta A_y^{\rm expt}(\theta_i)}\right]^2\\&+\left[\frac{\sigma_T^{\rm expt}-\sigma_T^{\rm calc}}{\Delta\sigma_T^{\rm expt}}\right]^2,\end{aligned} \tag{9}$$

where χ^2/N is the average chi square per data point, $\sigma^{\rm expt}(\theta_i)$ is the experimental cross section measured at θ_i, $\sigma^{\rm calc}(\theta_i)$ is the cross section calculated from the optical-model potential, $\Delta\sigma^{\rm expt}(\theta_i)$ is the error in the experimental cross section, and N_σ is the number of experimental cross-section points and similarly for the observables $A_y(\theta)$ and σ_T. At any energy one can insert a weight factor inside the bracket for any set of the observables in Eq. (9), and if the weighting factors are greater than unity, the total χ^2 per point increases artificially. Since the amount of $A_y(\theta)$ data was appreciably less than $\sigma(\theta)$ data and since we were interested in stressing the determination of the features of the spin-orbit potential, the $A_y(\theta)$ data were given a weight of 2. In the iteration procedure, values of one or more parameters are varied using the automatic search feature to minimize χ^2. A total χ^2/N was calculated for the entire data set when data for more than one energy were employed in extensive searches.

2. Individual fits

In the initial stage, optimum potential parameters were obtained in a separate search at each energy. Starting parameters for searching on the 4.0–6.5-MeV data were the ^{208}Pb parameters reported by Annand, Finlay, and Dietrich [3], while the starting parameters for the 7.0–40.0-MeV data were the ^{208}Pb parameters with linear energy dependences reported by Finlay *et al.* [4]. Contrary to most other analyses for ^{208}Pb(n,n), an imaginary spin-orbit term was included in our analysis. All potential-well strengths were searched upon first, followed by geometrical parameters, and finally by potential strengths and geometrical parameters simultaneously.

In order to provide spin-orbit parameters for energies where only cross-section data were available, energies at which $A_y(\theta)$ were available were searched upon first. Using the results of these single-energy searches, mean values of the strength, radius, and diffuseness of the real spin-orbit potential were obtained. In these searches at energies where $A_y(\theta)$ data exist, the value of the imagi-

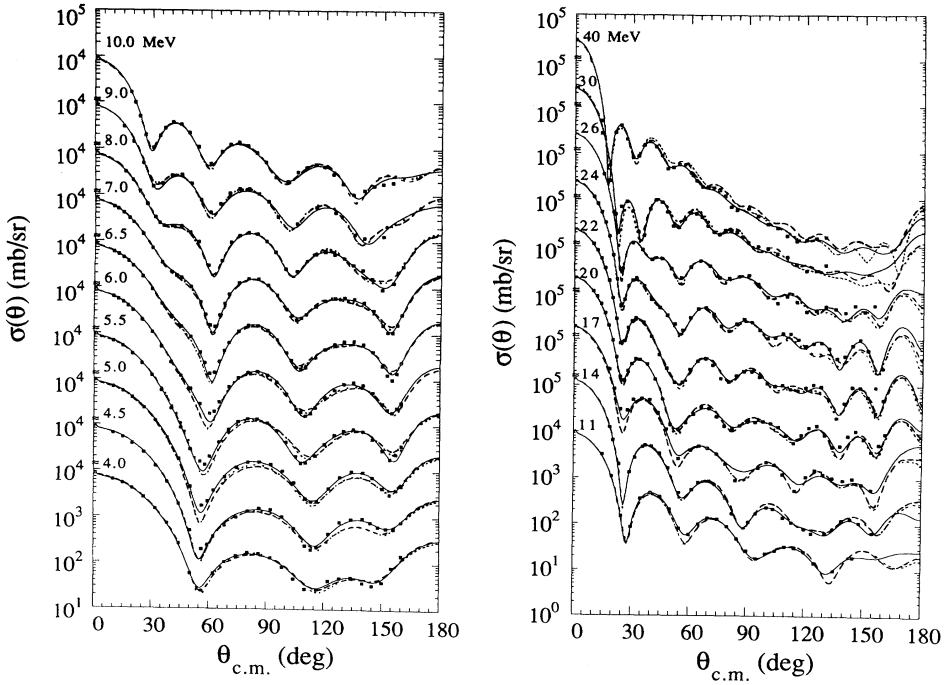

FIG. 9. Optical-model calculations using parameters from Table I compared with $\sigma(\theta)$ data (solid curves, best fits; long-dashed curves, constant geometry; and short-dashed curves, E-dependent geometry; where the short-dashed curve is not evident, it lies under the long-dashed curve). The data from 4.0 to 7.0 MeV have been adjusted for CN contributions.

nary spin-orbit strength was positive and ranged between 0.4 and 1.3 MeV. However, it showed no well-defined energy dependence. Therefore, for the searches at the energies where only cross-section data exist, it was decided to fix the strength $W_{\text{s.o.}}$ to have a linear energy dependence such that the depth was 0.6 MeV at $E=0$ and 0.0 MeV at $E=40$ MeV. This energy dependence was based on earlier SOM studies at TUNL and forces the $W_{\text{s.o.}}$ to have a strength of about -0.68 MeV at $E=80$ MeV, a strength close to the -0.65 MeV obtained by Schwandt *et al.* [23] for ^{208}Pb(p,p) scattering.

Final SOM parameters for the individual (single-energy) fits, which we categorize as "best fits," are listed in Table I, and the corresponding calculations are shown in Figs. 9 and 10. Table I also contains the volume integral per nucleon defined as

$$\frac{J}{A}=-\frac{1}{A}\int V(r)d^3r \ . \tag{10}$$

Except at 14.0 MeV, at all energies below 17 MeV the volume absorption W_V favored negative values. In the search process we set the strength to be zero at such energies. (See Table I.) For the present single-energy searches, the sum over all points and all energies of χ^2 for $\sigma(\theta)$, $A_y(\theta)$, and σ_T is 5200.

3. *Constant-geometry fits*

In order to examine the energy dependence of the real and imaginary potentials in a consistent way, for SOM studies below 40 MeV, traditionally one assigns constant

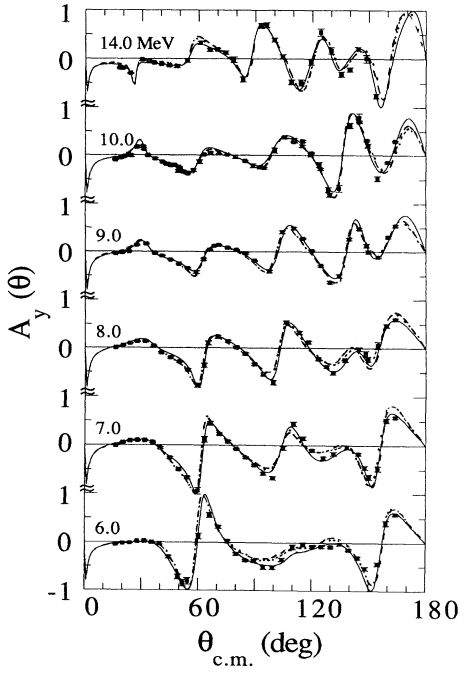

FIG. 10. Optical-model calculations using parameters from Table I compared to $A_y(\theta)$ data (solid curves, best fits; long-dashed curves, constant geometry; and short-dashed curves, E-dependent geometry; where the short-dashed curve is not evident, it lies under the long-dashed curve). The data at 6.0 and 7.0 MeV have been adjusted for CN contributions.

TABLE I. Single-energy $n+^{208}$Pb optical-model parameters.

E (MeV)	V_V (MeV)	r_V (fm)	a_V (fm)	W_V (MeV)	W_S (MeV)	r_I (fm)	a_I (fm)	$V_{s.o.}$ (MeV)	$r_{s.o.}$ (fm)	$a_{s.o.}$ (fm)	$W_{s.o.}$ (MeV)	J_V/A (MeV fm^3)	J_W/A (MeV fm^3)	χ^2/N_S	χ^2/N_P
4.0	47.373	1.222	0.726	0.000	6.240	1.302	0.351	6.583[a]	1.147[a]	0.488[a]	0.536[a]	398.04	31.71	1.36	
4.5	47.617	1.207	0.789	0.000	6.480	1.355	0.308	6.583[a]	1.147[a]	0.488[a]	0.528[a]	392.87	31.24	2.62	
5.0	44.436	1.272	0.662	0.000	6.511	1.343	0.300	6.583[a]	1.147[a]	0.488[a]	0.520[a]	412.25	30.03	1.67	
5.5	41.766	1.313	0.748	0.000	9.073	1.388	0.325	6.583[a]	1.147[a]	0.488[a]	0.512[a]	432.15	48.44	2.85	
6.0	43.122	1.289	0.672	0.000	8.425	1.338	0.316	6.590	1.256	0.349	1.279	416.42	40.65	6.88	6.07
6.5	43.666	1.275	0.666	0.000	9.015	1.333	0.311	6.583[a]	1.147[a]	0.488[a]	0.496[a]	408.19	42.48	7.20	
7.0	43.602	1.271	0.670	0.000	7.820	1.306	0.375	5.710	0.956	0.434	0.601	404.30	42.76	3.43	5.09
8.0	43.715	1.263	0.675	0.000	8.512	1.304	0.388	5.664	1.003	0.595	0.484	398.54	48.04	3.49	5.07
9.0	44.907	1.232	0.738	0.000	8.242	1.281	0.440	7.037	1.235	0.503	0.720	387.24	51.05	5.61	4.52
10.0	45.220	1.225	0.726	0.000	7.224	1.285	0.506	6.892	1.201	0.523	0.522	382.59	51.95	12.55	9.62
11.0	43.729	1.262	0.585	0.000	9.244	0.923	0.490	6.583[a]	1.147[a]	0.488[a]	0.424[a]	390.40	33.60	0.42	
14.0	44.664	1.226	0.743	0.497	7.402	1.276	0.526	7.611	1.230	0.526	1.081	380.37	59.18	5.03	4.32
16.9	41.289	1.266	0.655	0.000	8.292	1.205	0.523	6.583[a]	1.147[a]	0.488[a]	0.329[a]	377.34	54.36	26.59	
20.0	43.672	1.218	0.718	1.627	6.318	1.254	0.515	6.583[a]	1.147[a]	0.488[a]	0.280[a]	362.85	58.18	5.57	
22.0	44.976	1.189	0.715	2.211	4.789	1.301	0.542	6.583[a]	1.147[a]	0.488[a]	0.248[a]	348.87	59.27	5.75	
24.0	46.483	1.152	0.722	2.027	3.726	1.297	0.663	6.583[a]	1.147[a]	0.488[a]	0.216[a]	330.55	56.00	8.91	
25.7	43.251	1.195	0.725	2.321	4.836	1.278	0.580	6.583[a]	1.147[a]	0.488[a]	0.189[a]	341.17	61.09	3.30	
30.3	43.489	1.159	0.693	4.135	0.794	1.500	0.413	6.583[a]	1.147[a]	0.488[a]	0.115[a]	312.12	66.01	1.97	
40.0	37.390	1.240	0.752	5.434	4.291	1.274	0.527	6.583[a]	1.147[a]	0.488[a]	−0.040[a]	329.49	80.97	3.90	

[a]These parameters were held constant in the search.

values to the geometrical parameters and linear energy dependences to potential strengths. The geometrical parameters can be assigned either by averaging the values found in the individual fits or by searching for values that provide the best overall fit to the complete data set. A combination of both approaches was adopted here.

For the starting parameters of the initial searches, the best single-energy fits were used to determine average geometrical parameters and to produce a linear least-squares fit to the potential strengths. The imaginary spin-orbit potential was taken as the linear energy-dependent function used previously in the best-fit searches of the cross-section data. The entire data set was fit simultaneously, while holding the geometrical parameters constant and allowing the potential strengths to vary linearly with energy. As the search proceeded, we found that the strength of the real spin-orbit potential could be held constant without deleterious effects. The parameters resulting from the final search are given in Table II, while corresponding fits to $\sigma(\theta)$ and $A_y(\theta)$ are shown in Fig. 9 and 10 as long-dashed curves. The averaged ^{nat}Pb σ_T data are compared to the predictions for ^{208}Pb in Fig. 11. The total χ^2 of 12 200 obtained in this global search of the 4.0–40.0-MeV data set can be compared to the value of 5200 obtained in the best-fit searches.

Comparisons for χ^2 between the present model and the constant-geometry model of Annand, Finlay, and Dietrich [3] for the energy region from 4 to 11 MeV are, respectively, 7050 vs 13 200, and the constant-geometry model of Finlay *et al.* [4] for 7–50 MeV are 9020 vs 16 900. (For comparison, the parameters of Finlay *et al.* [4] are included in Table II.)

4. *Energy-dependent geometry fits*

Following their optical-model fits to scattering data from 4 to 40 MeV, Annand, Finlay, and Dietrich observed that the radius of the real central potential and the radius and diffuseness of the imaginary central potential prefer some variation with energy. In order to investigate these energy dependences for our more complete

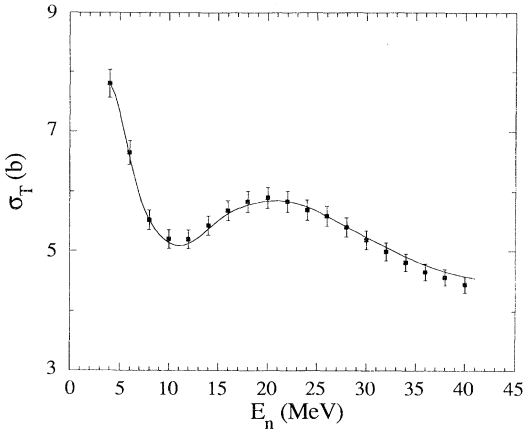

FIG. 11. Comparison of the averaged total cross-section data for $n+^{nat}$Pb to optical-model predictions for $n+^{208}$Pb using the constant-geometry parameters listed in Table II.

data set, we performed a search in which the geometries, as well as the potential strengths, were permitted to vary linearly with energy. Starting parameters were the same linear least-squares fits used initially in the constant-geometry search. The strength of the imaginary spin-orbit potential was held fixed to the linear energy dependence discussed earlier. Optical-model parameters resulting from this search are given in Table II, while corresponding fits are shown in Figs. 9 and 10 as short-dashed curves. For $E<25$ MeV the σ_T calculation obtained here is nearly identical to the curve shown earlier in Fig. 11; for $E>25$ MeV the calculated values are about 1% higher than the curve in Fig. 11.

The χ^2 obtained for the present model is about 6% less than that obtained with the constant-geometry model. However, there is a reluctance on our part to introduce four new energy dependences in order to achieve such a small reduction in χ^2. It is interesting to note, however, that when an energy-dependent geometry is introduced into the real central potential, the strength of the real central potential becomes nearly energy independent.

TABLE II. Optical-model parameters for $n+^{208}$Pb scattering.[a]

Parameter	Constant geometry	Finlay *et al.* [4]	*E*-dependent geometry
V_V (MeV)	$46.727-0.230E$	$49.130-0.310E$	$45.299-0.083E$
r_V (fm)	1.245	1.205	$1.277-0.003E$
a_V (fm)	0.690	0.685	$0.640+0.005E$
W_V (MeV)	0.0 for $E<10.5$	0.0 for $E<11.2$	0.0 for $E<10.5$
	$-1.845+0.176E$ for $E>10.5$	$-2.030+0.180E$ for $E>11.2$	$-1.110+0.112E$ for $E>10.5$
W_S (MeV)	$2.744+0.544E$ for $E<10.5$	$1.326+0.470E$ for $E<10.7$	$4.057+0.447E$ for $E<10.5$
	$10.031-0.150E$ for $E>10.5$	$7.752-0.130E$ for $E>10.7$	$10.284-0.146E$ for $E>10.5$
r_I (fm)	1.294	1.283	$1.321-0.002E$
a_I (fm)	0.450	0.499	$0.344+0.008E$
$V_{s.o.}$ (MeV)	6.112	5.750	6.152
$r_{s.o.}$ (fm)	1.174	1.105	1.178
$a_{s.o.}$ (fm)	0.517	0.499	0.541
$W_{s.o.}$ (MeV)	$0.600-0.016E$	0.000	$0.600-0.016E$

[a]Here E is the neutron energy in the laboratory system expressed in MeV.

This ambiguity between an energy dependence in the strength and an energy dependence in the geometry has also been noted by both Annand, Finlay, and Dietrich and JHM.

For completeness we mention that in the energy-dependent geometry model of Annand, Finlay, and Dietrich, the discrete values for the real and imaginary potential strengths were reported at each energy; these strengths were not parametrized with a single energy-dependent function. However, even with our constraint of requiring the strengths to vary linearly with energy, χ^2 for our model is about a factor of 2 better than that of the model of Annand, Finlay, and Dietrich.

V. DISPERSION-RELATION OPTICAL MODEL

A. Formalism and background

The average potential $V(r,E)$ is expected to be a continuous function of energy which varies smoothly as the nucleon energy E changes sign. When E is positive, $V(r,E)$ represents the real part of the optical-model potential, and when E is negative, it represents the shell-model potential. Through the dispersion relation, data from all energies can be utilized for parametrizing $V(r,E)$. This feature is especially useful for formulating the shell-model potential because the limited amount of data available for negative E can be augmented by the abundant and varied scattering data for positive E. Essentially, the information for negative E reduces to the energies of the single-particle bound states. The primary aim of the work described in this section is to deduce an optical-model potential which spans the region from positive to negative energies. In the first part we compare the known single-particle bound-state energies predicted by our model to the reported experimental bound-state values. Later, we use these known energies as an additional constraint.

The energy dependence of $V(r,E)$ is quite complicated in the region near the Fermi energy, the energy which separates the occupied and unoccupied single-particle states at negative energies. The energy dependence can be described in terms of the dispersion relation, which connects the real and imaginary parts of the optical-model potential and which occurs because the target does not remain in its ground state during the elastic-scattering process. In the dispersion relation, the real part of the optical-model potential is written as

$$V(r,E)=V_{\rm HF}(r,E)+\Delta V_S(r,E)+\Delta V_V(r,E)\ , \qquad (11)$$

where $V_{\rm HF}(r,E)$, $\Delta V_S(r,E)$, and $\Delta V_V(r,E)$ are the Hartree-Fock (HF), surface dispersive, and volume dispersive contributions to the mean field, respectively [1]. The dispersive contributions $\Delta V_S(r,E)$ and $\Delta V_V(r,E)$ are connected to the imaginary surface (W_S) and imaginary volume (W_V) parts of the optical-model potential (OPM) by the dispersion relations

$$\Delta V_S(r,E)=\frac{\rm P}{\pi}\int_{-\infty}^{+\infty}\frac{W_S(r,E')}{E'-E}dE'\ , \qquad (12)$$

$$\Delta V_V(r,E)=\frac{\rm P}{\pi}\int_{-\infty}^{+\infty}\frac{W_V(r,E')}{E'-E}dE'\ , \qquad (13)$$

where P denotes a principal-value integral.

While the energy dependence of $V_{\rm HF}(r,E)$ is expected to vary monotonically, this is not the case for $\Delta V_S(r,E)$ and $\Delta V_V(r,E)$. The rapid decrease of $W_S(r,E)$ and $W_V(r,E)$ with decreasing energy due to threshold effects causes $\Delta V_S(r,E)$ and $\Delta V_V(r,E)$ to have complicated energy dependences in the vicinity of the Fermi energy.

Satchler [24] pointed out that the addition of a derivative WS function (i.e., a surface term) and a WS volume function with the same radius parameter (i.e., $r_S\equiv r_V$) yields another WS volume function with a new radius parameter r_V', where r_V' where $r_V'>r_V$ if the depth of the surface term has the same sign as that of the volume term. This convenient result simplifies analyses that explicitly introduce the dispersion relation, but it also complicates the problem of distinguishing a surface contribution from a volume contribution. However, this result could explain why some analyses that ignore the DR exhibit an increasing radius $r_V(E)$ as $E\rightarrow 0$, since the DR correction ΔV_S adds constructively to the volume term in this energy region.

The approach followed here for the DR analysis is similar to that employed by Johnson, Horen, and Mahaux (JHM), where the imaginary potentials are assumed to have reflection symmetry about the Fermi energy. We note that the recent work by Finlay *et al.* [8] also focuses on the DR and draws conclusions from investigating volume integrals of the real and imaginary potentials. Most of the present analysis was completed before publication of Ref. [8]; however, the results of the present analysis tend to reinforce the conclusion of the $n+^{208}$Pb portion of their paper. A comprehensive overview of recent developments in the dispersive optical-model formulation is given in the review by Mahaux and Sartor [25].

B. Optical-model search

In preparation for implementing the dispersion relation, another optical-model search was performed in which the entire data set from 4.0 to 40 MeV was fit simultaneously. A constant geometry and a linear energy dependence on V was required, as in our earlier search. However, two new additional conditions were applied. First, the geometry of the imaginary volume potential was set identical to the geometry of the real volume potential. This was done so that the strength of the volume dispersive contribution to the mean field could be added directly to the strength of the Hartree-Fock potential. Second, the strength of the imaginary spin-orbit potential was taken to be zero. This was done in order to avoid the difficulty in computing single-particle bound-state values with a nonzero value for the imaginary spin-orbit potential strength. The appropriate starting parameters for this search were taken from our constant-geometry set of Table II.

After convergence, the new W_S and W_V were used in

Eqs. (12) and (13) to calculate the surface and volume dispersive contributions to the mean field, and the HF component of $V(r,E)$ was determined using Eq. (11). The code GENOA was then modified to include explicitly $V_{\rm HF}(r,E)$ of Eq. (11) and to require it to be an exponentially decreasing function [6] of $(E-E_F)$, where the Fermi energy E_F was chosen to be -6.0 MeV, as in Ref. [6]. The strength and exponential coefficients were inserted into GENOA as search parameters. The potential $V(r,E)$ was thereby represented in the search as the right-hand side of Eq. (11). Throughout the search process the dispersive contributions were recalculated according to Eqs. (12) and (13). The iterative process was repeated until no improvement was seen in the fits to the scattering data. Final parameters are listed in Table III. The $V_{\rm HF}$ obtained in this search (on only the scattering data) is labeled as "potential A" in Table III. The corresponding fits to the $\sigma(\theta)$ and $A_y(\theta)$ data are shown by the solid curves in Figs. 12 and 13. Optical-model predictions of $\sigma_T(E)$ for ^{208}Pb are shown in Fig. 14 in comparison to energy-averaged data of Larson, Hetrick, and Harvey [20] for $^{\rm nat}$Pb and data of Schutt *et al.* [21] for ^{208}Pb. Energy dependences of $V_{\rm HF}$, $V_{\rm HF}+\Delta V_V$, W_V, ΔV_V, W_S, and ΔV_S are shown in Fig. 15.

To compute single-particle bound-state energies, the real part of the Hartree-Fock optical-model potential $V_{\rm HF}(r,E)$ was extended to energies below E_F. The Hartree-Fock potential was approximated by a linear extrapolation of the $V_{\rm HF}(E)$ formula in Table II:

$$V_{\rm HF}(E)=46.338-0.261(E-E_F) \quad \text{for } E<E_F \ . \tag{14}$$

Using the computer code BOUNDSTATE (provided by C. Johnson of Oak Ridge National Laboratory), eigenvalues associated with $V(r,E)$ were calculated and compared to experimental energies of the weakly and deeply bound single-particle valence and hole states. Table IV lists the neutron bound-state energies (E_{nlj}) predicted by our extrapolated optical model compared to the empirical values based on separation energies, neutron single-particle states in ^{209}Pb, and single neutron-hole states in ^{207}Pb. In Table IV the left-hand column specifies the principal, orbital, and total angular momentum quantum numbers. Experimental values of the single-particle bound-state energies were taken from Table III of Johnson, Horen, and Mahaux [6] and are listed in the column labeled "Experimental E_{nlj}." The column labeled "Extrapolated $V_{\rm HF}$" lists the Hartree-Fock potential

TABLE III. Optical-model parameters for $n+^{208}$Pb obtained in the dispersion-relation analysis.

Parameter[a]	Value
$V_{\rm HF}$[b]	potential A: $46.338\exp[-0.261(E-E_F)/46.338]$ potential B: $47.591\exp[-0.332(E-E_F)/47.591]$ for $E>E_F$ $47.591-0.332(E-E_F)$ for $E<E_F$
$r_{\rm HF}$	1.221
$a_{\rm HF}$	0.720
W_V	0.0 for $E<11.4$ MeV $-2.032+0.178E$ for $11.4<E<50.7$ MeV 7.0[c] for $E>50.7$ MeV
r_{W_V}	$=r_{\rm HF}$
a_{W_V}	$=a_{\rm HF}$
ΔV_V	calculated from Eq. (12) and W_V above
W_S	$2.966+0.512E$ for $E<10.5$ MeV $9.749-0.134E$ for $10.5<E<72.8$ MeV 0.0 for $E>72.8$ MeV
r_{W_S}	1.291
a_{W_S}	0.463
ΔV_S	calculated from Eq. (11) and W_S above
$V_{\rm s.o.}$	6.214
$r_{\rm s.o.}$	1.147
$a_{\rm s.o.}$	0.546

[a]Potential strengths are in MeV and geometries are in fm.
[b]For both potentials A and B, $E_F=-6.0$ MeV.
[c]In order to apply the dispersion relation to the $n+^{208}$Pb data set, the value of $W_V(E)$ for $E>40$ MeV is needed. From fits to total cross section data, Johnson, Horen, and Mahaux [6] determined that W_V is approximately 7 MeV at 80 MeV. Therefore, $W_V(E)$ was parametrized by our linear expression up to $E=50.7$ MeV, and beyond this the constant value of $W_V(E)=7.0$ MeV was used.

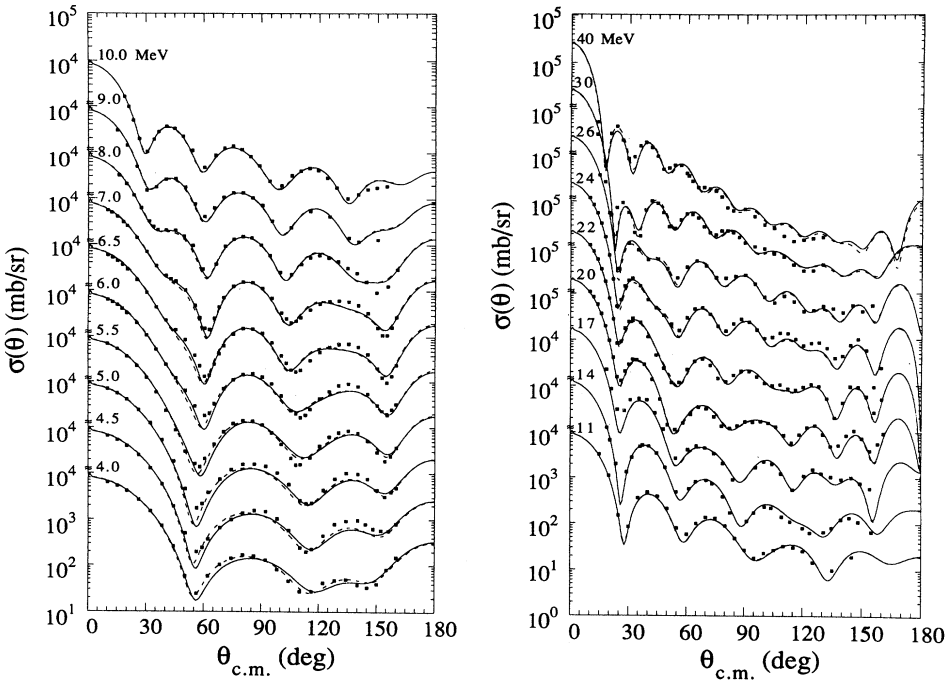

FIG. 12. Dispersion-relation optical-model calculations compared to $\sigma(\theta)$ data. Curves are calculations based on a global fits. The solid curves are from a fit to scattering data only, while the dashed curves are also based on information from bound-state energies (see text). Where the dashed curve is not evident, it lies under the solid curve. The data from 4.0 to 7.0 MeV have been adjusted for CN contributions.

strengths from $V_{\rm HF}$ (set A) and Eq. (13). Predicted bound-state energies are listed under "Predicted E_{nlj}."

For the next stage we used the experimental bound-state information to determine a potential that would give a better fit to the combined database (scattering plus bound state); we first calculated the strength for $V_{\rm HF}$ that yields the observed E_{nlj} exactly. For this all the other parameters, including the contributions ΔV_V and ΔV_S, were taken from Table III. At each energy where we had scattering data, we also obtained the values for $V_{\rm HF}$ that produce the best fit when the rest of Table III is used. These two sets of potential strengths were then fit using a

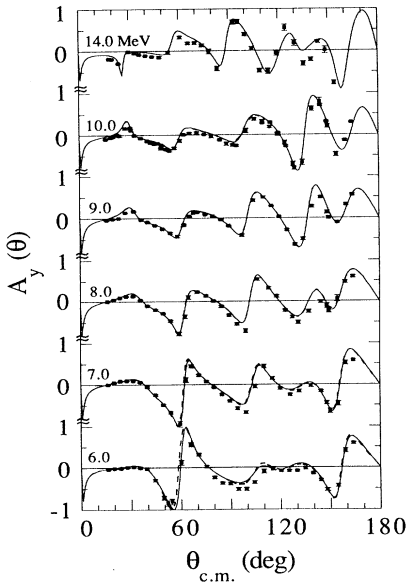

FIG. 13. Optical-model calculations compared to $A_y(\theta)$ data. See caption of Fig. 12. The data at 6.0 and 7.0 MeV have been adjusted for CN contributions.

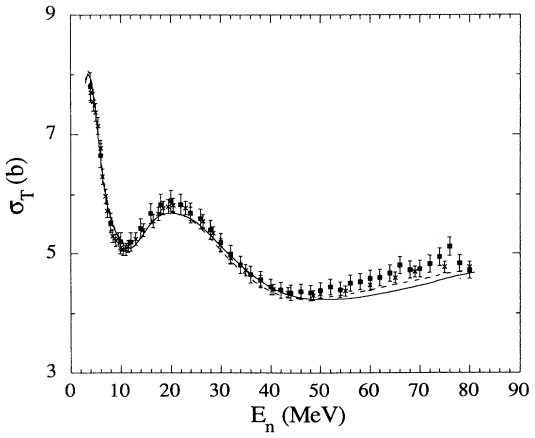

FIG. 14. Dispersion-relation optical-model predictions of the ^{208}Pb total cross section compared to the data. The solid curve is a prediction based on a global fit to scattering data only, while the dashed curve is based also on bound-state energies. The data are for $^{\rm nat}$Pb (solid circles) from Ref. [20] and for ^{208}Pb (crosses) from Ref. [21].

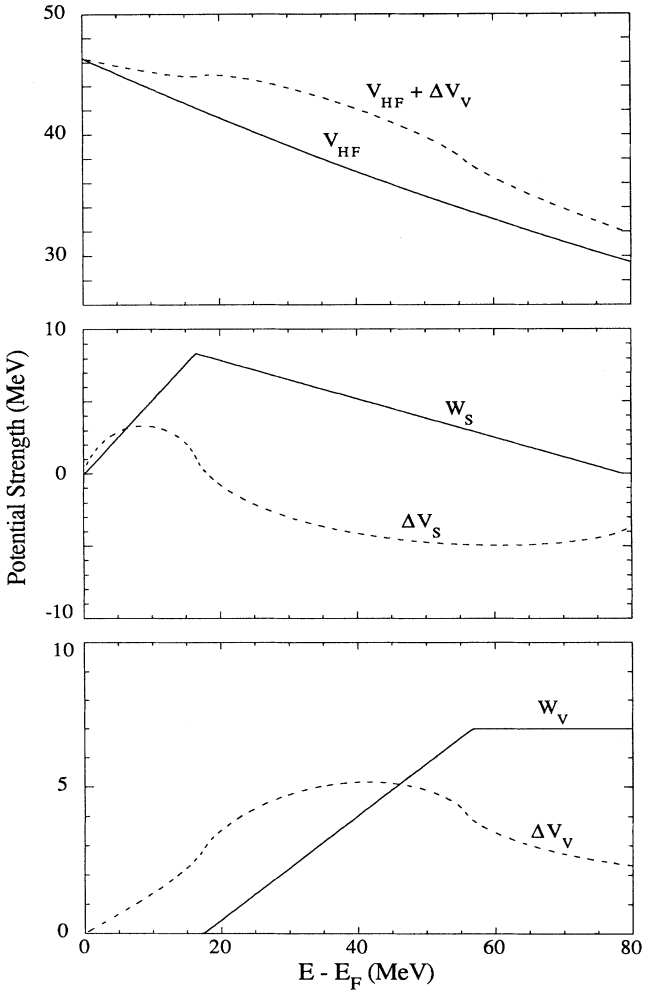

FIG. 15. Energy dependences of the Hartree-Fock (V_{HF}), Hartree-Fock plus volume dispersive ($V_{HF}+\Delta V_V$), imaginary volume (W_V), volume dispersive (ΔV_V), imaginary surface (W_S), and surface dispersive (ΔV_S) parts of the optical-model potential.

linear least-squares routine to obtain the optimum parametrization of the complete database. This V_{HF} is given in Table III as set B. (In this stage of analysis, no other parameters were searched upon.) Using this new Hartree-Fock potential, the bound-state energies and scattering data were recalculated. The column labeled "Fit" lists the Hartree-Fock potential strengths at the bound-state energies using set B. Predicted bound-state energies using this new Hartree-Fock potential are listed in the column labeled "Fit E_{nlj}." The neutron single-particle energies (at $E > E_F$) for $n + {}^{208}$Pb and single-hole energies (at $E < E_F$) for a neutron removed from ^{208}Pb are drawn in Fig. 16 for graphic illustration of the agreement of the measured energy-level diagram to that predicted by the models of Table III. Additional improvement in the fit might have been obtained if the spin-orbit parameters had been allowed to move from those of Table III and, particularly, if an energy dependent $V_{s.o.}$ was permitted; however, this option was not pursued. Fits to $\sigma(\theta)$ and $A_y(\theta)$ are shown as dashed curves in Figs. 12 and 13, while the predicted σ_T is shown as a dashed curve in Fig. 14. The total χ^2 for fits to the 4.0–40.0-MeV $n + {}^{208}$Pb scattering data set increased from 14 500 to 16 100 when using V_{HF} of set B. [Although it is not shown here, the JHM dispersion-relation model predicts similar bound-state energies as our "Fit V_{HF}"; the χ^2 for the 4–40 MeV scattering data with their model is about 25% larger (20 400), however. These calculations for 6–10 MeV are illustrated below.]

C. Comparison of the scattering data with the DR models of JHM and JJM

In this section we compare the 6–10-MeV data with calculations using the constant-geometry dispersion-relation (DR) models of JHM [6] and JJM [7]. We focus on the data in this energy range as this is the range of the new measurements. The two models will be denoted as DR (JHM) and DR(JJM). They differ only in that the

TABLE IV. Neutron single-particle and single-hole bound-state energies and strengths of the Hartree-Fock potentials.

nlj	Experimental E_{nlj} (MeV)	Extrapolated V_{HF} (MeV)	Predicted E_{nlj} (MeV)	Required V_{HF} (MeV)	Fit V_{HF} (MeV)	Fit E_{nlj} (MeV)
$^3d_{3/2}$	−1.40	45.153	−1.02	45.983	46.088	−1.45
$^2g_{7/2}$	−1.44	45.163	−0.94	46.047	46.101	−1.47
$^4s_{1/2}$	−1.90	45.280	−1.38	46.480	46.249	−1.80
$^3d_{5/2}$	−2.37	45.400	−1.78	46.536	46.401	−2.30
$^1j_{15/2}$	−2.51	45.436	−1.02	47.682	46.446	−1.69
$^1i_{11/2}$	−3.16	45.603	−1.70	47.583	46.657	−2.47
$^2g_{9/2}$	−3.94	45.803	−3.25	46.886	46.912	−3.96
$^3p_{1/2}$	−7.37	46.696	−6.70	47.691	48.046	−7.61
$^2f_{5/2}$	−7.94	46.844	−7.21	47.837	48.235	−8.24
$^3p_{3/2}$	−8.26	46.928	−7.41	48.156	48.341	−8.39
$^1i_{13/2}$	−9.00	47.121	−7.24	49.461	48.587	−8.34
$^2f_{7/2}$	−9.71	47.306	−9.46	47.639	49.823	−10.61
$^1h_{9/2}$	−10.78	47.586	−9.70	48.877	49.178	−10.88
$^1h_{11/2}$	−16.50	49.079	−14.76	51.228	51.077	−16.38

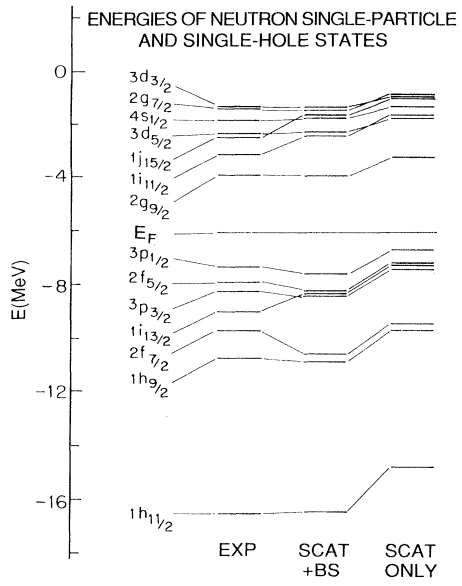

FIG. 16. Neutron-particle and neutron-hole states. Compared are experimental values (EXP) obtained from data tables, predicted values (SCAT) using the SOM based on scattering data only, and predicted values (SCAT+BS) using the SOM based on scattering data and bound-state energies (see text).

imaginary surface potential in DR(JJM) is l dependent, which, of course, through the DR, makes the dispersive surface potential also l dependent. The l dependency was attributed to two groups of l values: group (b) for $l=1$, 3, and 6 and group (c) for $l\neq 1$, 3, and 6. All potentials were assumed to have Woods-Saxon form factors and are given as

$$V_{\rm HF}(E)=-46.4\exp[-0.31(E-E_F)/46.4] \text{ for } E>E_F ,$$

$$r_{\rm HF}=r_{W_V}=1.240 \text{ fm} ,$$

$$a_{\rm HF}=a_{W_V}=0.68 \text{ fm} ,$$

$$W_V(E)=-0.17(E-10) \text{ MeV for } 10<E<50 \text{ MeV} ,$$

$$W_V(E)=-6.8 \text{ MeV for } E>50 \text{ MeV} ,$$

$$V_{\rm s.o.}=5.75 \text{ MeV} ,$$

$$r_{\rm s.o.}=1.105 \text{ fm} ,$$

and

$$a_{\rm s.o.}=0.50 \text{ fm} .$$

The imaginary surface potential for the DR(JHM) consists of line segments

$$W_S(E)=-0.4(E-E_F) \text{ MeV for } -6<E<10 \text{ MeV} ,$$

$$W_S(E)=0.103(E-72) \text{ MeV for } 10<E<72 \text{ MeV} ,$$

and

$$W_S(E)=0 \text{ for } E>72 \text{ MeV} .$$

For the l-dependent DR(JJM), the corresponding segments for the (b) group are

$$W_{\rm Sb}(E)=0 \text{ for } -6<E<-2 \text{ MeV} ,$$

$$W_{\rm Sb}(E)=-0.7959(E+2) \text{ MeV for } -2<E<6.5 \text{ MeV} ,$$

$$W_{\rm Sb}(E)=-0.1033(72-E) \text{ MeV for } 6.5<E<72 \text{ MeV} ,$$

$$W_{\rm Sb}(E)=0 \text{ MeV for } E>72 ,$$

and, for the (c) group,

$$W_{\rm Sc}(E)=0 \text{ for } -6<E<-5 \text{ MeV} ,$$

$$W_{\rm Sc}=-0.3646(E+5) \text{ MeV for } -5<E<12 \text{ MeV} ,$$

$$W_{\rm Sc}(E)=-0.1032(72-E) \text{ MeV for } 12<E<72 \text{ MeV} ,$$

and

$$W_{\rm Sc}(E)=0 \text{ for } E>72 .$$

The real surface geometry was set equal to that of the imaginary surface, i.e., $r_{W_S}=r_{V_S}=1.27$ fm and $a_{W_S}=a_{V_S}=0.58$ fm. The calculations were performed using the computer code GENOA modified to include l-dependent surface terms. In Figs. 17 and 18 the calculated curves are compared with the $\sigma(\theta)$ and $A_y(\theta)$ data, respectively. The 6- and 7-MeV data are corrected for CN contributions. The dashed curves represent the DR(JHM) and the solid the DR(JJM). As can be seen in these figures, the DR(JJM) tends to improve the agreement with the data, more so for the cross sections, which were the only data available at the time that the models were developed.

None of the constant-geometry DR models lead to precise "fits" of the data and, especially, simultaneous fits to both $\sigma(\theta)$ and $A_y(\theta)$ as good as those which were achieved with our "best-fit," single-energy OMP searches

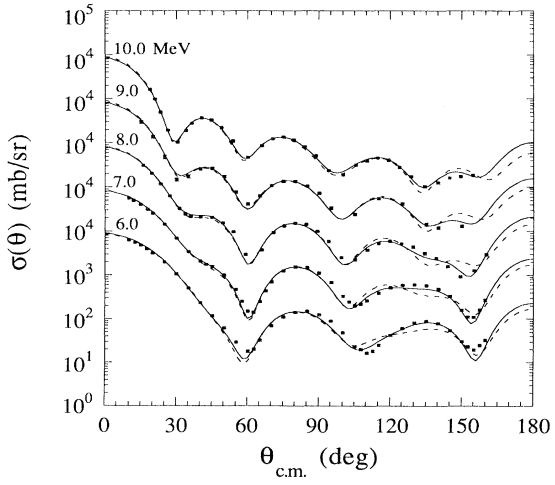

FIG. 17. $\sigma(\theta)$ compared to earlier DR models. The solid curve represents predictions for the l-dependent JJM model and the dashed curve for the JHM model.

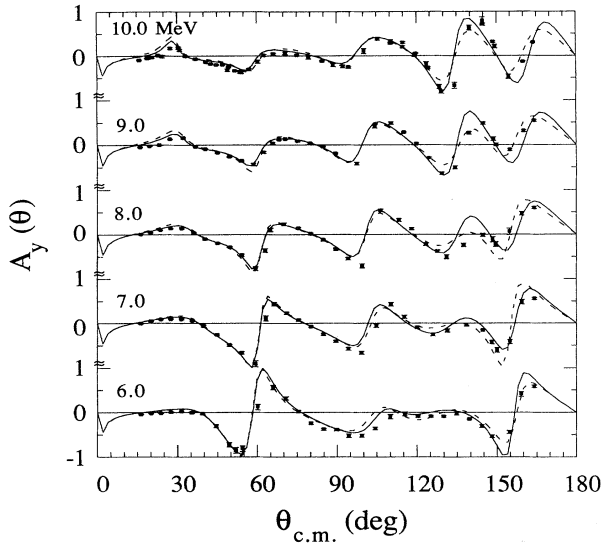

FIG. 18. $A_y(\theta)$ data compared to earlier DR models. See caption of Fig. 17.

that resulted in the parameter sets given in Table I. We have performed numerous searches in the 6–10-MeV range starting with the DR parametrizations in an effort to determine whether precise fits could be obtained with small adjustments to the parameters. In all of these efforts, the imaginary volume potential was kept equal to zero. The searches involved (a) adding a Fourier-Bessel term to the real potential of the DR(JHM), (b) searching on all the potential depths of the DR(JJM), (c) searching on single potential terms [i.e., both depth and geometry of the DR(JJM)], and (d) searching on the geometries of the DR(JJM). In none of these searches did we obtain precise fits to the data. Those which showed significantly improved fits were accompanied by relative changes in parameters at the 2% level, i.e., changes in magnitudes which were comparable to the dispersive correction terms. From searches on the 7-MeV data, it was clear that improved fits to $\sigma(\theta)$ and $A_y(\theta)$ could only be achieved with smaller values of the surface diffuseness.

Finally, we compared the data to the l-dependent DR model of JHM that has an energy-dependent a_{W_S} and a_{V_S}. This model, in which the integral of the real surface potential is related to the integral of the imaginary surface potential through the DR constraint, was shown to yield the best fits to the scattering data below about 10 MeV. Although this model does not rigorously satisfy the DR because the true radial shape of the real surface potential does not conform to a WS form factor, it has been shown [7] to yield $\sigma(\theta)$ values which are similar to those derived from an l-dependent DR model with a weak energy-dependent a_{W_S} and with a $\Delta V_S(r,E)$ that was deduced from $W_S(r,E)$ by numerical integration.

VI. SUMMARY AND CONCLUSIONS

We have measured $\sigma(\theta)$ for elastic and inelastic neutron scattering at 8.0 MeV on ^{208}Pb and $A_y(\theta)$ for elastic and inelastic scattering at 6.0, 7.0, 8.0, 9.0, and 10.0 MeV. These measurements have been utilized in conjunction with previously measured $\sigma(\theta)$, $A_y(\theta)$, and σ_T data to obtain an accurate data set for neutron elastic scattering from ^{208}Pb from 4.0 to 40.0 MeV. Various models were used to describe this data set. We first performed searches on the data at separate energies using conventional optical-model analyses. In these, the real volume, imaginary volume ($E > 17.0$ MeV), imaginary surface, and real and imaginary spin-orbit potentials had Woods-Saxon form factors. Best fits were obtained by allowing essentially all of the parameters (i.e., potential depths and geometries) to vary in the search at each energy. These resulted in fairly good simultaneous fits to all the data. Although the deduced parameters did not exhibit a smooth dependence with incident neutron energy, there was an indication of some trend in some of the geometrical parameters (e.g., the radius of the real volume potential).

We next proceeded to seek a global fit using fixed geometries and energy-dependent strengths. The detailed fits to the differential scattering and analyzing power data were poorer than those obtained from the individual "best fits," although σ_T between 4.0 and 40.0 MeV was still quite well reproduced.

A global search was performed in which the geometrical parameters of the real volume, imaginary volume, and imaginary surface potentials were allowed to vary linearly with energy. This parametrization gave fits similar to those attained with the global search with constant geometries.

Overall, our global fits, which include the new data, are similar to those achieved by Annand, Finlay, and Dietrich [3] in their analysis over the smaller energy range 4–11 MeV. Although both of these parametrizations seem to reproduce the kinematic trends in the data, they do not yield precise fits or fits that are as good as the best fits attained for the data at each energy.

The new $A_y(\theta)$ data help to constrain the spin-orbit parameters. In the above global models we found that the data were described quite well by a s.o. potential which had a constant strength for the real part. The data also show evidence for a need for an imaginary s.o. potential with a strength of the same sign as the real part.

A dispersion-relation analysis similar to that reported by JHM was performed, except here we have used an iterative global method of search and included the analyzing power data. Our resulting $V_{\rm HF}(r,E)$ potential differed slightly from that of JHM; i.e., we found $V_{\rm HF}(E_F)=47.591$ vs 46.4 MeV and $r_V=1.221$ vs 1.240 fm, respectively. The fits to the data were quite similar.

We have also compared the data with the $A_y(\theta)$ calculated using the constant-geometry DR models with (JJM) and without (JHM) l dependence in the imaginary surface potential. The l-independent DR(JHM) tends to reproduce the features of the data, but does not provide good fits, especially below about 10 MeV. However, the l-dependent DR(JJM) noticeably improves the fits.

We then use the DR(JHM) and DR(JJM) parametrizations as starting conditions and sought to determine whether more precise fits to the scattering and analyzing

power data at each energy in the 6.0–10-MeV region could be obtained. It was found that where significant improvements in the fits resulted, the varied parameters changed by the order of 2% (i.e., changes comparable in magnitude to the DR corrections).

Finally, we have found that the $\sigma(\theta)$ and $A_y(\theta)$ data at 6.0 and 7.0 MeV could be better fit by the l-dependent, energy-dependent diffuseness DR model of JHM. Although this model does not strictly satisfy the DR, it predicts cross sections that are in good agreement with a rigorous DR model of a similar type (i.e., l-dependent, weak energy-dependent diffuseness model of JJM). The fits achieved by this model are comparable to the best fits attained with searches using a SOM with WS form factors.

Hence, although use of the DR constraint with WS form factors is reasonably successful at predicting the $n+^{208}$Pb dynamics in the energy regions from about -20 to 40 MeV and leads to a simple understanding of the OMP parameters, the requirement of energy dependence in the geometry of the imaginary surface potential to more precisely fit the scattering data below about 15 MeV introduces complexities which make a DR analysis difficult. This is especially so because the form of the real surface potential can no longer be described at all energies with a WS form factor. The origin of this energy dependence arises from the fact that the amplitudes of the different partial waves contain nodes in the nuclear surface region which tend to decouple the corresponding partial waves from excitation of collective surface modes [26]. Such excitations are the main contributor to the imaginary surface potential. The net result is to make the imaginary surface potential l and energy dependent [6,7]. In light of these difficulties, it is no wonder that Mahaux and Sartor [27] have opted to ignore this energy interval in their more recent applications of the moment approach to the DR.

A major problem to be faced in trying to deduce whether the data can be precisely fit with a self-consistent DR model is the lack of sensitivity at the (less than or proportional) 2% level of determining individual parameters. It is not clear whether assuming a WS form factor for the imaginary surface potential or an energy-independent spin-orbit potential is proper at this level of sensitivity. It is clear that to push the model beyond the simple fixed geometry representations will be difficult.

ACKNOWLEDGMENTS

We gratefully acknowledge a series of very informative calculations with C. H. Johnson and appreciate the use of his code BOUNDSTATE. We also acknowledge the assistance of K. Murphy, H. G. Pfutzner, and M. AlOhali in performing the measurement. This work is supported by the U.S. Department of Energy, Office of High Energy and Nuclear Physics, under Contract Nos. DE-AC05-76ER01067 with Duke University and DE-AC05-84OR21400 with Martin Marietta Energy Systems, Inc.

*Present address: Lawrence Livermore National Laboratory, P. O. Box 808, 1-397 Livermore, CA 94550.

†Permanent address: Department of Phyiscs, Tsinghua University, Beijing, China.

[1] C. Mahaux and H. Ngô, Nucl. Phys. **A378**, 205 (1982).

[2] H. Feshbach, Ann. Phys. (N.Y.) **5**, 357 (1958).

[3] J.R.M. Annand, R. W. Finlay, and F. S. Dietrich, Nucl. Phys. **A443**, 249 (1985).

[4] R. W. Finlay, J.R.M. Annand, T. S. Cheema, and J. Rapaport, Phys. Rev. C **30**, 796 (1984).

[5] J. Rapaport, T. S. Cheema, D. E. Bainum, R. W. Finlay, and J. D. Carlson, Nucl. Phys. **A296**, 95 (1978).

[6] C. H. Johnson, D. J. Horen, and C. Mahaux, Phys. Rev. C **36**, 2252 (1987).

[7] J.-P. Jeukenne, C. H. Johnson, and C. Mahaux, Phys. Rev. C **38**, 2573 (1988).

[8] R. W. Finlay, J. Wierzbicki, R. K. Das, and F. S. Dietrich, Phys. Rev. C **39**, 804 (1989).

[9] C. E. Floyd, Jr., Ph.D. dissertation, Duke University, 1981; C. E. Floyd, P. P. Guss, R. C. Byrd, K. Murphy, R. L. Walter, and J. P. Delaroche, Phys. Rev. C **28**, 1498 (1983).

[10] M. L. Roberts, Ph.D. dissertation, Duke University, 1988.

[11] S. M. El-Kadi, Ph.D. dissertation, Duke University, 1981; S. M. El-Kadi, C. E. Nelson, F. O. Purser, R. L. Walter, A. Beyerle, C. R. Gould, and L. W. Seagondollar, Nucl. Phys. **A390**, 509 (1982).

[12] C. R. Howell, Ph.D. dissertation, Duke University, 1984.

[13] G. G. Ohlsen and P. W. Keaton, Jr., Nucl. Instrum. Methods **109**, 41 (1973).

[14] P. W. Lisowski, R. L. Walter, C. E. Busch, and T. B. Clegg, Nucl. Phys. **A242**, 298 (1975).

[15] J. C. Hopkins and G. Breit, Nucl. Data Tables A **9**, 137 (1971).

[16] E. Woye (unpublished).

[17] R. C. Byrd, C. E. Floyd, K. Murphy, P. P. Guss, and R. L. Walter, Nucl. Phys. **A427**, 36 (1984).

[18] W. Tornow, C. R. Howell, M. L. Roberts, P. D. Felsher, Z. M. Chen, R. L. Walter, G. Mertens, and I. Slaus, Phys. Rev. C **37**, 2326 (1988).

[19] R. P. DeVito, Ph.D. dissertation, Michigan State University, 1979; R. P. DeVito, S. M. Austin, U.E.P. Berg, W. Sterrenberg, and L. E. Young, Nucl. Instrum. Methods **215**, 423 (1983).

[20] D. C. Larson, D. M. Hetrick, and J. A. Harvey, Bull. Am. Phys. Soc. **25**, 543 (1980); (private communication).

[21] R. L. Schutt, R. E. Shamu, P. W. Lisowski, M. S. Moore, and G. L. Morgan, Phys. Lett. B **203**, 22 (1988).

[22] The authors acknowledge R. Varner for recognizing an error in the earlier TUNL modifications described by Floyd in Ref. [9].

[23] P. Schwandt, H. O. Meyer, W. W. Jacobs, A. D. Bacher, S. E. Vigdor, M. D. Kaitchuck, and T. R. Donoghue, Phys. Rev. C **26**, 55 (1982).

[24] G. R. Satchler, in *Isospin in Nuclear Physics,* edited by D. H. Wilkinson (North-Holland, Amsterdam, 1969), p. 411.

[25] C. Mahaux and R. Sartor, Adv. Nucl. Phys. (to be published).
[26] D. J. Horen, C. H. Johnson, and A. D. MacKellar, Phys. Lett. **161B**, 217 (1985); D. J. Horen, C. H. Johnson, J. F. Fowler, A. D. MacKellar, and B. Castel, Phys. Rev. C **34**, 429 (1986).
[27] C. Mahaux and R. Sartor, Nucl. Phys. **A493**, 157 (1989).